Explicit simulation of cumulus ensembles with the GATE phase III data: Budgets of a composite easterly wave

By KUAN-MAN XU[1]* and DAVID A. RANDALL[2]
[1]*NASA Langley Research Center, USA*
[2]*Colorado State University, USA*

SUMMARY

The mass, heat and moisture budgets of a composite easterly wave over the eastern tropical Atlantic are analysed from simulations of a convection-resolving model (CRM). The large-scale data from the GARP (Global Atmospheric Research Program) Atlantic Tropical Experiment (GATE) phase III are used to drive the CRM simulations. The simulated, composite easterly wave is reasonably comparable with the observed, except for the lack of shallow convection embedded in the simulated easterly waves. The mesoscale stratiform precipitation processes are found to be an inseparable component of cumulus convection embedded in the easterly waves. Their main differences from convective processes are twofold: (1) the distinct vertical structures of the budget components due to mesoscale updraughts and downdraughts, and (2) the phase lags relative to the convective processes in the temporal evolution of the easterly waves. Thus, theoretical studies should include both convective and mesoscale stratiform precipitation processes in order to further understanding of diabatic processes in the dynamics of the easterly waves and possibly other waves in the tropics. In addition, the budget analysis presented in this study also provides some details for improving parametrizations of cumulus convection.

KEYWORDS: Cloud-resolving simulations Easterly waves GATE convection

1. INTRODUCTION

Easterly waves are westward-travelling tropospheric disturbances in the tropics (Rhiel 1954). These synoptic-scale disturbances occur most frequently in the summer hemisphere, with periods of 3–5 days and wavelenghts of 2000–5000 km. They arise through a mixed barotropic/baroclinic instability of the low-level easterly jet (e.g. Burpee 1972; Reed *et al.* 1977; Norquist *et al.* 1977; Lau and Lau 1992; Thorncroft and Hoskins 1994a,b; Thorncroft 1995; Paradis *et al.* 1995). The African easterly waves (AEWs) are initiated in the region of central and eastern Africa at ∼15°N and propagate across the Atlantic during the northern summer (Burpee 1972). They have far-reaching effects on the African climate and the Atlantic tropical cyclones (e.g. Landsea 1993).

The origin, structure and propagation characteristics of AEWs were extensively studied in the 1960s and 1970s with rawinsonde records from stations located in western Africa and the Caribbean islands, and through limited, short-term field experiments such as the Global Atmospheric Research Program's (GARP's) Atlantic Tropical Experiment (GATE). Burpee (1972, 1974) determined that the waves originate at 15°–30°E where the African easterly jet develops in response to the strong temperature gradient between the Sahara and equatorial Africa/Gulf of Guinea. He also noticed that the AEWs propagate westward along two east–west oriented tracks located at 15°–20°N and at 5°–10°N. The disturbances along the southern track are associated with moist convection while those along the northern track are associated with dry convection (Carlson 1969; Burpee 1974). The northern track dips southwards along the monsoon trough over the eastern Atlantic and eventually merges with the southern track (Reed *et al.* 1977).

Detailed AEW dynamic and thermodynamic structures, as well as the energetics, were identified during GATE, with the aid of a very dense network of rawinsonde soundings over the west of Africa and the eastern tropical Atlantic (e.g. Norquist *et al.* 1977; Reed *et al.* 1977; Thompson *et al.* 1979; Chen and Ogura 1982). Eight observed

wave disturbances during phase III and the preceding interphase period were composited by Reed and collaborators. The composite disturbance has the strongest wind at 650 mb, with a cold core below and a warm core above. Maximum low-level convergence and upward vertical motion are located in the region just ahead of the trough, along with the greatest convective cloud cover and largest precipitation rate. The temporal variations in convective activity cannot be explained thermodynamically because of the nearly out-of-phase relationship between conditional instability and convective intensity (Thompson *et al.* 1979). They are, however, linked to the associated variations in the large-scale divergences or vertical motions.

The energetics analysis by Norquist *et al.* (1977) showed that barotropic instability is the main energy source for the growth of the easterly waves in the GATE region, while baroclinic instability is the dominant energy source for the easterly waves over the African continent. Diabatic generation of available potential energy associated with latent-heat release is important for the waves over the eastern Pacific (Nitta 1970). Using a global dataset, Lau and Lau (1992) showed that diabatic generation in the eastern tropical Atlantic should, however, play a similar role as in the Pacific disturbances.

Nevertheless, the importance of diabatic processes in easterly wave dynamics and energetics has not yet been fully understood, due partly to poor representations of moist processes in theoretical studies. Although theoretical studies with prescribed latent heating are able to produce realistic-looking easterly waves (e.g. Holton 1971; Shapiro *et al.* 1988), such studies can only partly reveal the importance of diabatic processes in the wave dynamics because the interactions between the diabatic heating and wave dynamics were omitted. A wave-CISK* (Charney and Eliassen 1964; Ooyama 1964; Lindzen 1974) parametrization has often been used in theoretical studies, with or without conditional heating (e.g. Rennick 1976; Simmons 1977; Mass 1979; Kwon 1989; Kwon and Mak 1990; Thorncroft and Hoskins 1994a,b; Paradis *et al.* 1995).

On the other hand, parametrized latent-heat release that is based upon positive moisture convergence has strong impacts on the structures of the waves, but not on the characteristic parameters of the waves such as the phase speeds and wavelengths. Paradis *et al.* (1995) concluded that such parametrizations are insufficiently realistic.

Kwon and Mak (1990) showed that the transformation from cold-core easterly waves to warm-core tropical storms occurs only under the cumulative influence of strong cumulus heating during the westward propagation of the waves. No such transformation can occur using the unconditional heating of the wave-CISK theory. Thorncroft and Hoskins (1994a,b) found that the roles of latent heating are (i) to increase the baroclinic energy conversions relative to the barotropic energy conversions, and (ii) to determine the wave structures, using the same wave-CISK formulation as in Kwon and Mak (1990). Paradis *et al.* (1995) utilized a complete moist dynamics framework (i.e. moisture is prognostically determined) and confirmed the findings of Thorncroft and Hoskins (1994a,b). Paradis *et al.* (1995) emphasized that the upper-level circulations of simulated easterly waves are not realistically represented by a simple CISK-type parametrization with mean observed heating and drying profiles typical of the easterly waves (Reed and Recker 1971), although the structures are much more realistic than those of the dry easterly waves.

General-circulation model (GCM) simulations of AEWs have been performed by several groups (Estoque *et al.* 1983; Reed *et al.* 1988; Duvel 1990; Lau and Lau 1990; Druyan and Hall 1994; Fyfe 1999; Céron and Guérémy 1999). Reed *et al.* (1988) and Duvel (1990) analysed the easterly waves over West Africa and the tropical Atlantic,

---

* Conditional Instability of the Second Kind.

combining the European Centre for Medium-range Weather Forecasts (ECMWF) operational analysis data with satellite data. Lau and Lau (1990) performed a global analysis of the easterly wave disturbances using June–August 1980–87 ECMWF analyses. Druyan and Hall (1994) simulated AEWs with the Goddard Institute for Space Studies (GISS) GCM. They found that simulated waves exhibit realistic wavelengths but propagate westwards too slowly. Fyfe (1999) used the Canadian Centre for Climate Modeling and Analysis model to compare the modelled and re-analysed easterly waves. Although the GCM-simulated AEWs have comparable periods, wavelengths and energetics conversions with the waves in the re-analysed data sets, the southern track of the moist easterly waves is totally absent. Céron and Guérémy (1999) examined the ability of the Centre National de Recherches Métérologiques GCM to simulate the space–time variability of the AEWs. They found that both the northern and southern tracks cannot be simultaneously obtained. In summary, these studies have shown that not all aspects of the moist easterly waves can be simulated with GCMs although such analyses are necessary for evaluating GCM physics and dynamics.

From the discussion presented above, one can conclude that a much more thorough understanding of the roles that cumulus convection plays in the easterly waves is needed, and that new approaches should be proposed that would lead to a better understanding of easterly waves. Paradis *et al.* (1995) suggested a grid-nesting approach to resolve convection around the AEW trough; a convection-resolving model (CRM) is embedded in an AEW dynamical model so that a direct treatment of the scale interaction is possible. In the present study, a convection-resolving modelling approach is adopted without the two-way interactions between the AEWs and convection; the observed synoptic-scale conditions drive a CRM (or cloud ensemble model). The main motivation of this study is to improve the understanding of the roles of cumulus convection in the easterly waves.

The major objectives of this study are as follows: (1) to compare the CRM-simulated with the observed bulk properties of the fully mature and nonlinear easterly waves observed during GATE phase III; (2) to investigate the mass, heat and moisture budgets of the convective and stratiform regions of a composite easterly wave; and (3) to examine the roles of mesoscale stratiform precipitation processes and their relationship with convective processes in the easterly waves.

It should be pointed out that the feedbacks of cumulus convection on the easterly waves cannot be investigated in this study because synoptic-scale motions are prescribed in the CRM, i.e. synoptic-scale advective tendencies of temperature and moisture are used to drive the CRM to produce the response of cumulus convection. The main contribution of this study to the understanding of the easterly wave dynamics is to *diagnose* explicitly the effects of diabatic processes with a CRM, and to separate the contributions of convective and mesoscale stratiform precipitation processes to the budgets of a composite easterly wave. Such an approach is unprecedented in studying the easterly waves.

Because of its high quality, the GATE dataset has been extensively used in developing and evaluating parametrizations of cumulus convection (e.g. Lord and Arakawa 1980; Betts and Miller 1986; Tiedtke 1989; Gregory and Rowntree 1990; Donner 1993). As a by-product, the detailed budget analysis presented in this study will also contribute to improvement of the recently developed parametrizations that also explicitly treat the stratiform precipitation (e.g. Fowler *et al.* 1996; Ghan *et al.* 2000).

A major limitation of this study is the utilization of a two-dimensional (2-D) model. Although Donner *et al.* (1999) used a three-dimensional (3-D) CRM to study the life cycle of a composite easterly wave, the imposed synoptic-scale forcings on

their model are from the composite wave. Their approach limits the extent to which simulated convection arising from composite forcing can be compared with composite observations of individual easterly waves. The present approach of simulating the entire GATE phase III period, on the other hand, allows a straightforward comparison of simulations with composite observations by using an identical compositing procedure as in the observational study of Thompson *et al.* (1979) that is based upon the observed phase of the easterly waves.

The rest of the paper is organized as follows. Numerical simulations are briefly described in section 2; results are presented in section 3, and conclusions are given in section 4.

2. NUMERICAL SIMULATIONS

The details of the numerical simulations were described by Xu and Randall (1996). Briefly, the model used in this study is the 2-D (x and z) University of California–Los Angeles/Colorado State University (UCLA/CSU) CRM (Krueger 1988; Xu and Krueger 1991; Krueger *et al.* 1995; Xu and Randall 1995). The CRM is based on the anelastic system of dynamical equations with the Coriolis acceleration. It includes (a) a third-moment turbulence closure, (b) a three-phase bulk cloud microphysics, and (c) an interactive, broadband radiative transfer.

In the simulations, the observed large-scale destabilizing and moistening rates due to large-scale horizontal advection and large-scale vertical motion are imposed on the CRM grid points, uniformly in x. The simulated, domain-averaged wind components are nudged towards the observed winds because the simulated structures of the cloud systems are highly sensitive to the domain-averaged wind profiles. Nudging of the winds is necessary due to the inability of limited-area models to simulate the large-scale dynamics.

The control simulations described by Xu and Randall (1996) are analysed for this study, which was run for 18 days of physical time, from 1 to 18 September 1974, with a time step of 10 s. The dataset as analysed by Thompson *et al.* (1979) was used to provide information on observed large-scale conditions over a B-scale ship array with an area of approximate 90 000 km². The observed, daily-mean sea surface temperature (SST; Krishnamurti *et al.* 1976) is used in the simulation; the diurnal variation of the SST cannot be incorporated into the simulation because the required data are not available.

Three simulations are performed; two of them are initialized with perturbed initial temperature and moisture profiles with magnitudes of the perturbation of ±1 K for temperature and ±0.5 g kg⁻¹ for moisture. Such an ensemble of simulations provides multiple realizations of the cumulus ensemble under a given large-scale condition. Ideally, even more experiments should be performed with various perturbations in the initial conditions, because differences among the three simulations are rather random at a given instance, due to the internally non-deterministic nature of cumulus convection (Xu *et al.* 1992). Nevertheless, the averaged results over the three simulations are used to represent the easterly waves.

The remaining aspects of the simulations are as follows. The domain size is 512 km, with a horizontal grid size of 2 km. The vertical coordinate is stretched to give finer resolution near the surface, with 33 layers. The radiation module is called every 150 s using the 'accumulated' method proposed by Xu and Randall (1995). This allows a large time interval while the accumulated effects of clouds on radiation are approximately captured.

The results presented by Xu and Randall (1996) can be briefly summarized as follows. The observed time variations of the surface precipitation rate, surface evaporation rate, outgoing long-wave radiation flux, and the vertical distributions of temperature, water vapour mixing ratio and relative humidity were successfully reproduced by the model, as were the vertical structures and time evolutions of the major convective systems. The simulated temperature and specific-humidity departures from observations are generally small during the 18-day simulation (± 1 K and ± 1 g kg^{-1}), and seldom exceed 2 K and 1.5 g kg^{-1}, respectively. The 2-D simulation does have some limitations; for example, artificially strong inhibiting effects on convection, and unrealistically efficient vertical transports of heat, moisture and momentum when the vertical wind shear is strong. The latter was noticed by Soong and Tao (1980), who reduced the upper-tropospheric wind shear by 20% in their simulation of GATE rainbands.

In Xu and Randall (1996), the mass, heat and moisture budgets of the simulated cumulus ensembles were not analysed. The present study provides such analyses in the context of a composite easterly wave to better understanding of the roles of cumulus convection.

3. RESULTS

(a) Comparison with observations

The radar-estimated surface precipitation rate (Hudlow and Patterson 1979) and simulated precipitation rate for the composite easterly wave are first compared (Fig. 1). Compositing of data is accomplished by assigning each 3-hourly- and domain-averaged variable to one of eight wave categories in accordance with Table 1 of Thompson et al. (1979), except that the 30 and 31 August 1974 observations are excluded, because the CRM simulation starts from 1 September 1974 (Xu and Randall 1996). Thus, the observed results shown in this study are slightly different from those shown in Thompson et al. (1979).

The agreement between the simulated and observed precipitation rates is remarkably good except for a large overestimate for the wave category between the ridge (R) and northerly (N) phases (Fig. 1(a)). The simulated, maximum precipitation rate also appears at the trough (T) as in observations. The simulated surface evaporation rate also compares well with the estimate from the bulk method (Fig. 1(b)). These results are not surprising in view of the general agreement between simulation and observations during the 18-day simulation (Xu and Randall 1996). In spite of its weak variation, the surface evaporation rate reaches its maximum just before the R phase. It decreases thereafter and reaches its minimum between R and N. Thus, surface evaporation does not correlate well with the convective activity embedded in the easterly waves. Instead, there is a phase lag of approximately three wave categories (equivalent to 36 h).

The amounts of simulated and satellite-observed 'cold clouds' are compared in Fig. 2(a). The observations were from the GOES* Synchronous Meteorological Satellite (SMS-1) infrared images (Fig. 18 of Thompson et al. (1979)). The simulated cold-cloud fraction is defined for those CRM columns (2 km wide) for which the cloud-top temperature is less than 245 K, whereas the cloud top is the height where the top-downward integrated cloud water and ice path is equal to 0.02 kg m^{-2} (Harshvardhan et al. 1994; Cahalan et al. 1995; Poore et al. 1995). Thus, the cold-cloud amount measures the fraction of cumulonimbi and their associated upper-tropospheric anvils

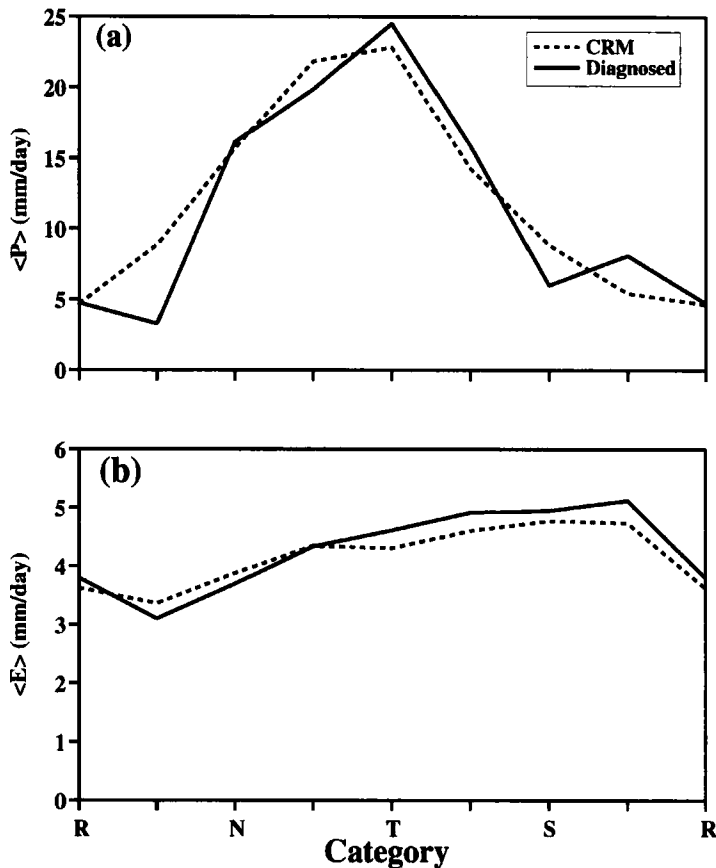* Geostationary Operational Environmental Satellite.

Figure 1. (a) Radar-estimated and convection-resolving model (CRM) simulated surface precipitation rates and (b) diagnosed and CRM simulated surface evaporation rates as functions of the phase of the composite easterly wave. See text for explanation of phase categories.

in the CRM domain. The lower-level anvils with temperatures between 273 and 245 K are, thus, excluded by such a definition.

The agreement between simulated and observed cold-cloud amounts is somewhat acceptable except for a weak temporal variation in the simulated cloud fraction, and a 10–15% underestimate around the trough and an equal amount of overestimates between R and N and at the southerly (S) phase (Fig. 2(a)). The overestimates of cold-cloud amount and surface precipitation rate between R and N are probably caused by (1) the temporal smoothing of the imposed large-scale advective forcings of the Thompson *et al.* (1979) dataset, and (2) the more inhomogeneous boundary layer associated with preceding waves that enables convection to be initialized more easily in the ridge phase in the model than observed. The overestimate of cold-cloud amount in the S phase may be related to the lack of horizontal export of condensate after the convective peak, due to the periodic lateral boundary conditions used in the model.

The total cloud fraction shows large underestimates for all wave categories except for around the ridge (Fig. 2(b)). This is related to the underestimate of the low-level cloud fraction as shown in Fig. 16(b) of Xu and Randall (1996). Xu and Randall (1996) suggested several reasons for the underestimate of the low-level cloud fractions: (1) the
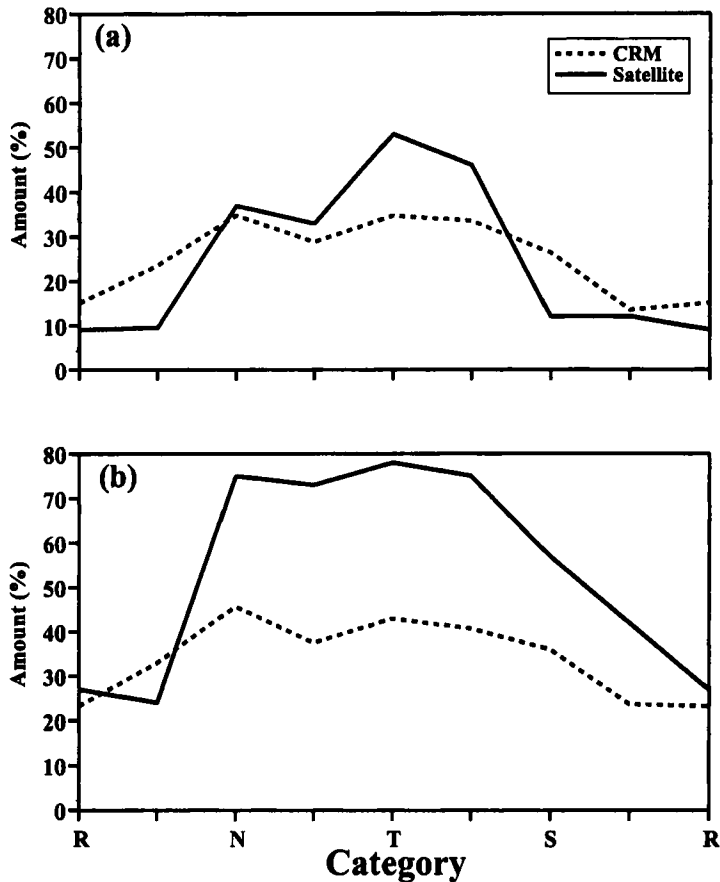
Figure 2. Satellite observed and convection-resolving model (CRM) simulated (a) cold-cloud amount and (b) total cloud amount as functions of the phase of the composite easterly wave. See text for explanation of phase categories.

neglect of rainwater/snow/graupel in defining the total cloudiness, (2) the coarse horizontal resolution used in the simulation, and (3) the omission of a subgrid-scale condensation parametrization in the simulation. An improvement of model physics and/or an increase of the horizontal spatial resolution are needed to address the underestimate of total cloud fraction.

The underestimates of the low-level cloud fraction are most likely to impact the surface radiative budgets. This could be a very serious problem if the CRM is coupled with an oceanic model. Additional impacts on the simulated easterly waves are discussed below.

The observed and simulated temperature and specific-humidity deviations from the mean state of the composite wave are shown in Fig. 3 as functions of height and the phase of the easterly waves. The simulated temperature deviations (Fig. 3(a)) agree somewhat with observations (Fig. 3(b)). The main differences between model and observation are that the simulated deviations have a much larger amplitude (0.4 K vs. 0.1 K) of the temporal evolution in the middle troposphere (3 to 10 km) and the warmer lower troposphere (below 4 km) between N and S.

The overall pattern of the simulated specific humidity deviations (Fig. 3(c)) also agrees somewhat with observations (Fig. 3(d)) except for the much smaller amplitudes
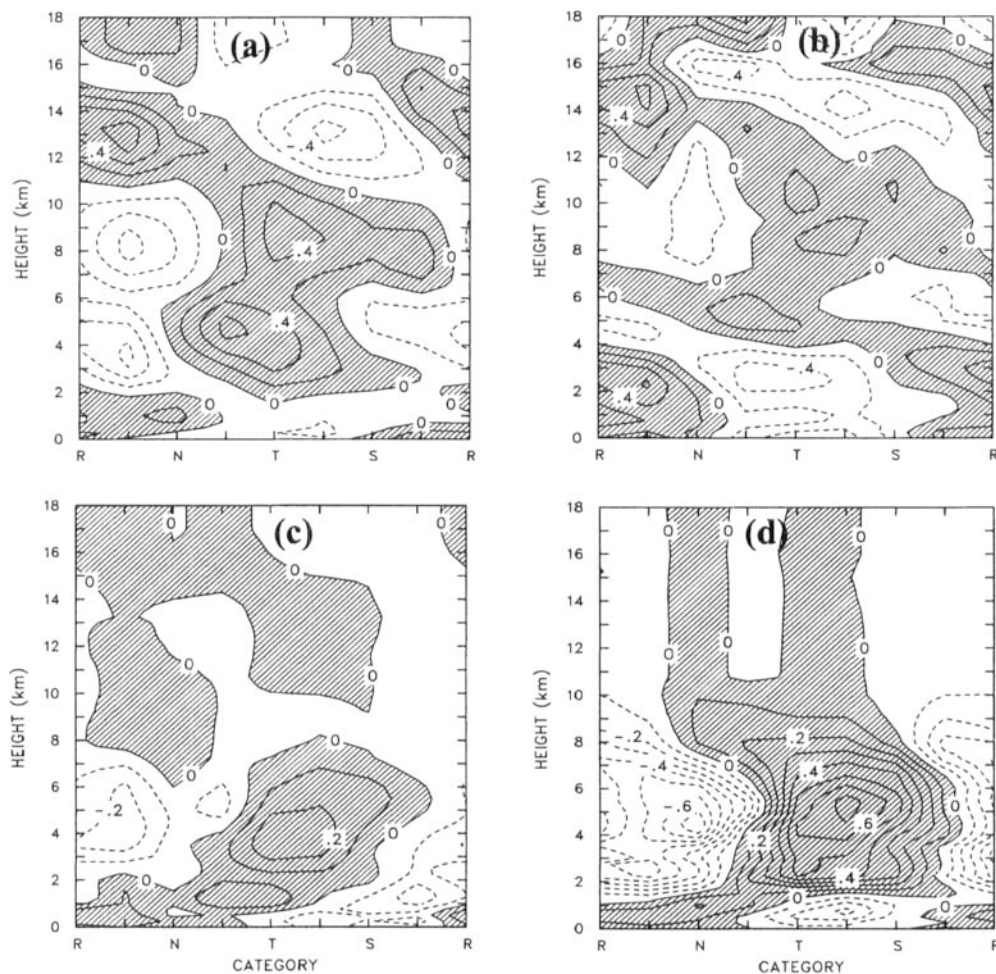
Figure 3. Wave phase–vertical cross-sections of (a) simulated and (b) observed temperature deviations, and (c) simulated and (d) observed specific-humidity deviations. The contour interval is 0.2 K in (a) and (b), and 0.1 g kg^{-1} in (c) and (d), respectively. Contours greater than 0 K or 0 g kg^{-1} are hatched. Negative values shown dashed. See text for explanation of phase categories.

of temporal variations for all wave categories (0.2 g kg^{-1} vs. 0.7 g kg^{-1}) and some phase differences in the middle troposphere.

There are several possible reasons for the differences in the thermodynamic structures between the simulated and observed easterly waves. The underestimate of shallow cumulus clouds in the model (see Fig. 16(b) in Xu and Randall (1996)) is a likely cause. This type of cloud produces cooling and moistening at its top through detrainment. By simulating more shallow clouds, i.e. more cooling and moistening in the lower troposphere, the temperature and specific-humidity deviations could be brought into better agreement with observations. Increasing the horizontal and vertical resolutions of the model could also result in stronger eddy transports of moisture, which could increase the shallow-cloud population. Deficiencies in the bulk cloud microphysics of the model (e.g. evaporation of raindrops) may be also responsible for the differences between the simulated and observed thermodynamic structures.

In summary, the simulated composite easterly wave is reasonably comparable with the observed, except for the lack of shallow cumulus convection. The temperature and specific-humidity departures from observations are almost an order of magnitude smaller than those obtained with similar CRM simulations with the GATE phase III dataset (Grabowski *et al.* 1996; Xu and Randall 1996; Donner *et al.* 1999), due primarily to cancellations resulting from the compositing procedure. It could be expected that the results presented below are not greatly affected by the small differences in the composited thermodynamic structures between simulation and observation.

(b)   Microphysical characteristics

The domain-averaged liquid and solid water mixing ratios are shown in Fig. 4 for cloud water, cloud ice, snow, graupel and rainwater, and their sum. The most distinct feature of Fig. 4 is the asymmetry across the trough; for example, all water species have much smaller mixing ratios between S and R than between R and N. Such an asymmetry suggests that convective processes dominate before the trough phase, in agreement with the 3-D CRM simulation of Donner *et al.* (1999). Further evidence in support of such an explanation is the occurrence of the maximum cloud water and rainwater mixing ratios immediately before the trough phase (Figs. 4(d) and (e)).

Another feature appearing in Figs. 4(a) and (b) is that the magnitudes of cloud ice mixing ratio and snow mixing ratio are smaller than those of other water species. The maximum cloud ice and snow mixing ratios appear slightly after the trough phase. This may suggest that stratiform precipitation is more active after the trough phase. The 'melting bands' at ~5 km are most apparent in graupel and total condensate mixing ratios (Figs. 4(c) and (f)).

On the other hand, a comparison of these simulated water species with observations is almost impossible due to a lack of observations (see Donner *et al.* (1999) for a detailed discussion). The composited maximum values shown in Fig. 4 are slightly smaller than other similar studies (Grabowski *et al.* 1996; Donner *et al.* 1999) because individual waves, instead of compositing of several waves, were simulated in those studies. In addition, the details of microphysics used in this study (three categories of ice) are different from those in the other studies (two categories of ice). Therefore, it would not be fair to conclude that the magnitudes of water species shown in Fig. 4 are more realistic that those in other studies.

(c)   Mass budget

For cumulus ensemble, continuity of mass requires:

$$\rho \overline{w} = M_c + \widetilde{M}. \qquad (1)$$

Here $\rho \overline{w}$ is the large-scale mass flux $(\overline{M})$, the overbar denotes the large-scale average, ρ is the density of the air, M_c is the cloud mass flux and $\widetilde{M}$ is the mass flux in the environment, i.e. the environmental subsidence. The cloud mass flux is the sum of the mass fluxes of all clouds, either saturated or unsaturated draughts with condensate. That is, M_c can be written as the sum of updraught mass flux, M_u, and downdraught mass flux, M_d:

$$M_c \equiv M_u + M_d. \qquad (2)$$

An updraught is always saturated while a downdraught can be saturated or unsaturated (with precipitation). A saturated grid cell with positive (negative) vertical velocity is defined as an updraught (downdraught). Thus, M_u does not include the upward motion
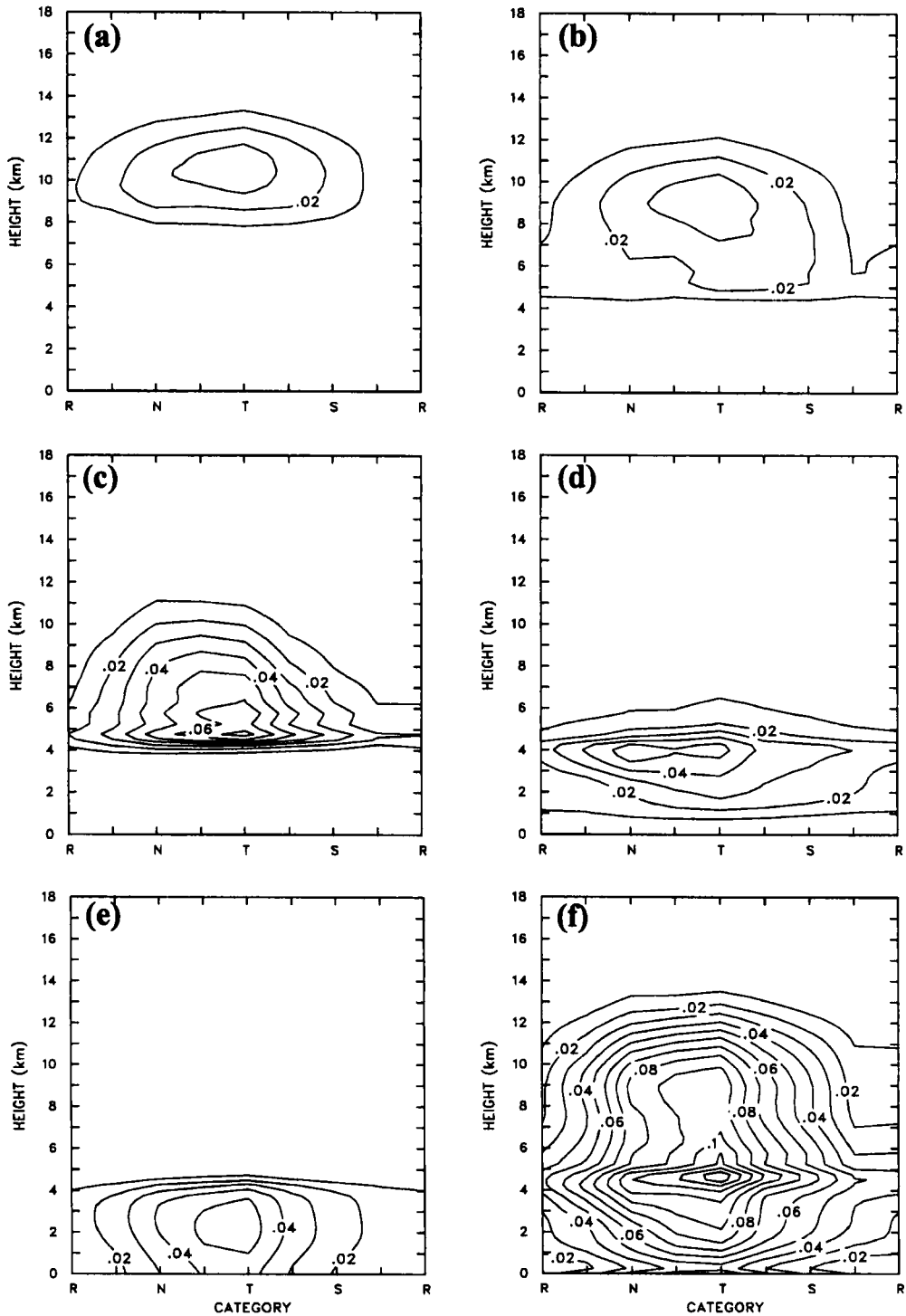
Figure 4.   Wave phase–vertical cross-sections of simulated (a) cloud ice, (b) snow, (c) graupel, (d) cloud water, (e) rainwater and (f) total condensate mixing ratios. The contour interval is 0.01 g kg^{-1}. See text for explanation of phase categories.
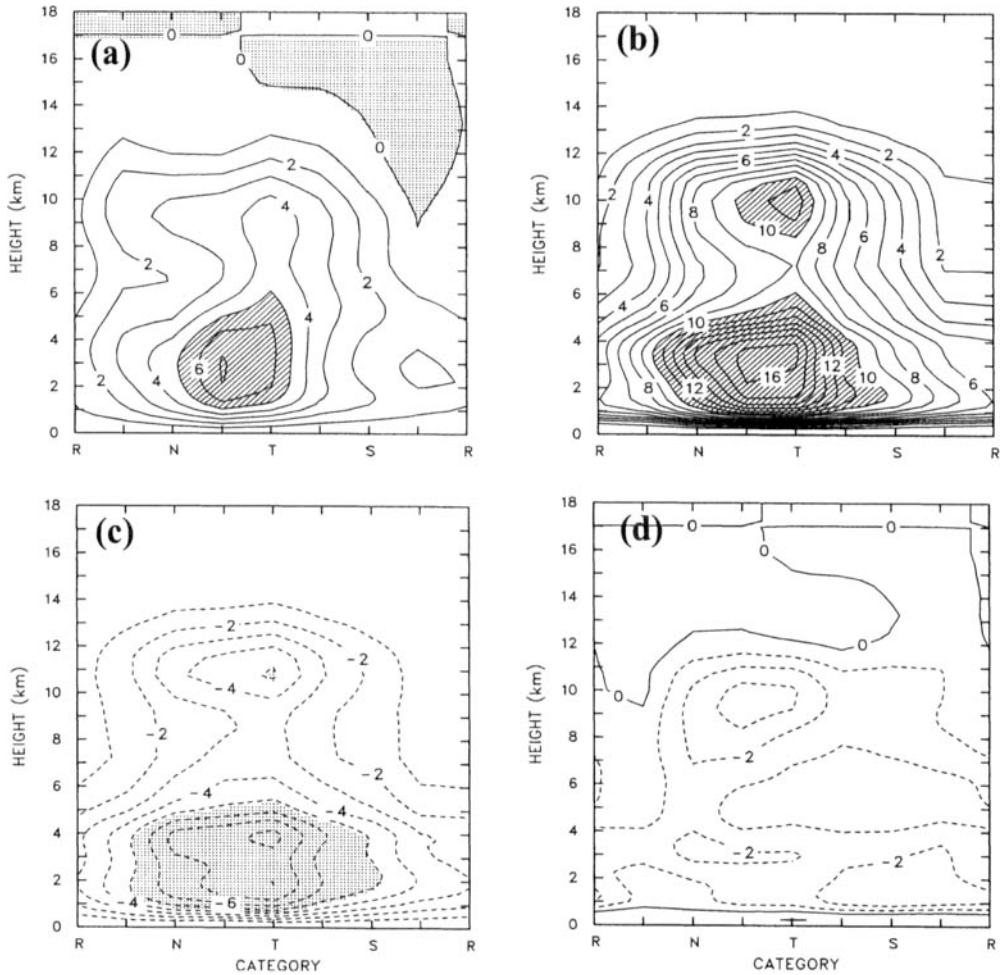
Figure 5. Wave phase–vertical cross-sections of (a) large-scale mass flux $(\overline{M})$, (b) updraught mass flux (M_u), (c) downdraught mass flux (M_d) and (d) environmental subsidence $(\widetilde{M})$. The contour interval is 1 mb h^{-1}. Contours less than 0 and -5 mb h^{-1} are dotted in (a) and (c), respectively. Contours greater than 5 and 10 mb h^{-1} are hatched in (a) and (b), respectively. Negative values are shown dashed. See text for explanation of phase categories.

at unsaturated grid cells. The environment is defined as any grid cell without any liquid water/ice. Detailed criteria used in this study can be found in Xu (1995).

The domain-averaged mass budget components, as expressed by (1) and (2), are shown in Fig. 5, which include $\overline{M}$, M_u, M_d, and $\widetilde{M}$. The large-scale mass flux exhibits a distinct phase lag between the lower and middle/upper troposphere (Fig. 5(a)). The maximum large-scale ascents occur in the lower troposphere earlier (between N and T) with a magnitude of 7 mb h^{-1}, and later in the upper troposphere with a magnitude of 4 mb h^{-1}. The reason for this is discussed below.

The updraught mass flux, M_u, shows a pattern similar to that of $\overline{M}$ except with much greater magnitudes, i.e. by a factor of 2–3 (Fig. 5(b)). This indicates that downdraughts and the environmental subsidence are required to satisfy the mass balance. In addition, the maximum centre of M_u at 10 km is much more pronounced than that of $\overline{M}$, due to the upper tropospheric anvils or mesoscale updraughts. This maximum is partially
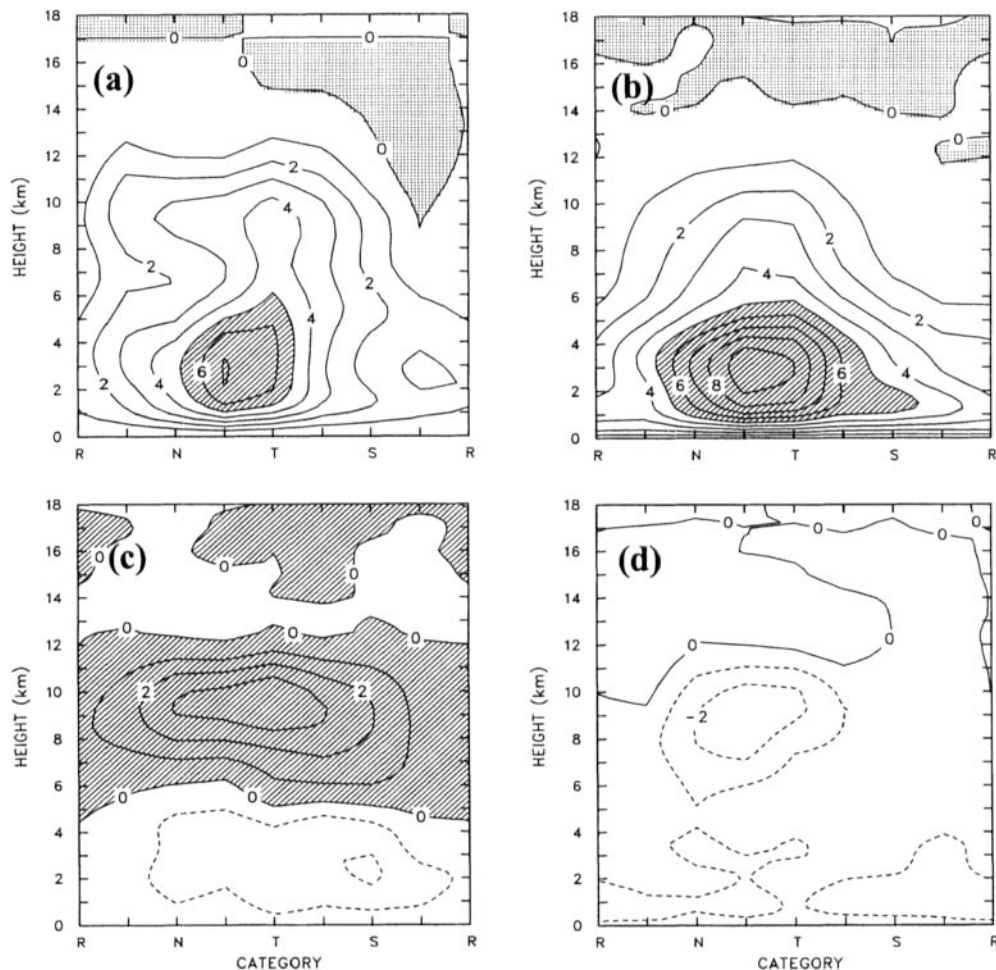
Figure 6. Wave phase–vertical cross-sections of the averaged mass flux over (a) the entire domain $(\overline{M})$, (b) convective regions $(\overline{M}_{conv})$, (c) stratiform regions $(\overline{M}_{strt})$ and (d) clear regions $(\overline{M}_{clr})$. The contour interval is 1 mb h^{-1}. Contours less than 0 mb h^{-1} are dotted while contours greater than 5 mb h^{-1} are hatched in (a) and (b). Contours greater than 0 mb h^{-1} are hatched in (c). Negative values are shown dashed. See text for explanation of phase categories.

counterbalanced by downdraught mass flux, M_d (Fig. 5(c)), which is largely associated with saturated draughts (Xu 1995). The maximum centres of M_u and M_d in the upper troposphere could be partially due to the presence of gravity-wave reflection from the upper boundary of the model. On the other hand, the downdraught mass flux in the lower troposphere is related to unsaturated, precipitation-driven downdraughts. It should be pointed out that the magnitudes of M_u and M_d are probably 20–30% too large, due to the two-dimensionality of the model (Lipps and Hemler 1986; Tao and Soong 1986). However, the general vertical structure, except for the gravity-wave contributions in the upper troposphere, and the temporal evolution, can be trusted.

The large-scale subsidence, $\widetilde{M}$, occurs below 12 km, with a maximum magnitude of 3 mb h^{-1} (Fig. 5(d)), which is almost half as large as $\overline{M}$. The temporal evolution of $\widetilde{M}$ is not modulated as strongly by the wave as the other components of the mass budget. This

suggests that radiative processes are driving the large-scale subsidence of the composite easterly wave although the contribution of convective processes cannot be ruled out.

The domain-averaged mass budget can also be expressed as the sum of the total mass fluxes in the convective, stratiform and clear regions ($\overline{M}_{conv}$, $\overline{M}_{strt}$, and $\overline{M}_{clr}$; Fig. 6). The partitioning of convective and stratiform regions follows that proposed by Xu (1995), which was based on the strength of updraughts and downdraughts. An entire CRM column is classified as one of the three regions: convective, stratiform or clear. By definition, a clear region does not have any condensate in the column. Also note that $\overline{M}_{conv}$ and $\overline{M}_{strt}$ are basically free from the gravity-wave contributions because the mass fluxes of saturated updraughts and downdraughts produced by gravity-wave reflections cancel each other.

The total mass flux in the convective region (Fig. 6(b)) shows positive values up to 14 km with a maximum centre at 3 km and just before the trough phase. This coincides with the observed $\overline{M}$ but with much larger spread of the 5 mb h^{-1} contour over five wave categories (Fig. 6(b)). This suggests that convective circulations/processes are highly modulated by the large-scale vertical motion (Xu *et al.* 1992) since the latter is prescribed in the simulation. Unlike $\overline{M}$, there is almost no vertical phase tilting in $\overline{M}_{conv}$ (Fig. 6(b)).

Figure 6(c) shows that $\overline{M}_{strt}$ changes sign at approximately 5 km, reflecting the characteristics of mesoscale precipitating anvils embedded in the easterly waves (e.g. Houze 1977). Houze (1977) and many others have shown such characteristics for mesoscale convective systems (MCSs). The result of Fig. 6(c) is, however, shown in the context of a composite easterly wave.

The maximum centre at 9.5 km occurs at the trough while the minimum centre at 3 km occurs at the S phase (Fig. 6(c)). Such a phase difference of the maximum/minimum centres (approximately 24 h) is related to the slow development of mesoscale downdraughts as anvils become mature. It should be noted that the time lag is much shorter for individual MCSs.

It is apparent that the vertical structure of $\overline{M}_{strt}$ contributes to the maximum $\overline{M}$ at around 9 km at the trough phase. Comparison of Fig. 6(b) with Fig. 6(c) suggests that there is a phase difference of the maximum centres between convective and stratiform processes as far as the total mass fluxes in both regions are concerned. This explains the characteristics of $\overline{M}$ mentioned earlier, because both convective and stratiform processes contribute to the observed large-scale mass fluxes.

The total mass flux in the clear region ($\overline{M}_{clr}$), i.e. excluding the convective and stratiform columns, shows negative values in the lower and middle troposphere (Fig. 6(d)). The negative centres occur before the trough phase, which suggests that they are induced by convective processes. On the other hand, the magnitude of $\overline{M}_{clr}$ is smaller than that of $\overline{M}$ (Fig. 5(d)) because the latter also includes some contributions (~ 1 mb h^{-1}) from the stratiform regions but negligible contributions from the convective regions (not shown).

To understand further the relationships among $\overline{M}$, $\overline{M}_{conv}$ and $\overline{M}_{strt}$, lagged correlation coefficients are calculated from hourly and domain-averaged mass fluxes (Fig. 7). A range of lag times from -12 to $+12$ h is chosen. The range is equivalent to two wave-phase categories. A positive lag time indicates that the large-scale mass flux precedes the convective (stratiform) mass flux. There is a high correlation between $\overline{M}$ and $\overline{M}_{conv}$ for a range of lags in the lower and middle troposphere (Fig. 7(a)) and between $\overline{M}$ and $\overline{M}_{strt}$ in the middle and upper troposphere. The most important feature of Fig. 7(a) is the tilting of the maximum correlation axis with height. Because both $\overline{M}_{conv}$ and $\overline{M}_{strt}$
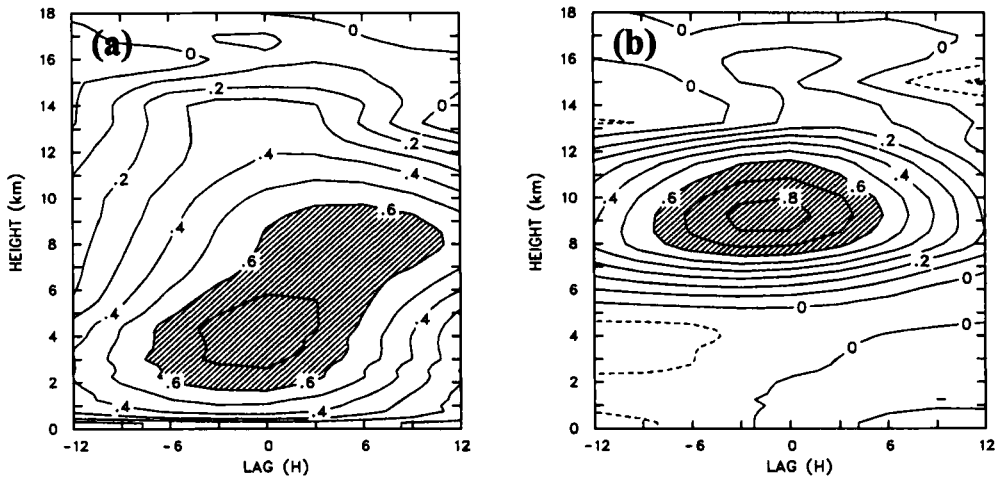
Figure 7.   Lag correlations (a) between the total mass flux in convective regions ($\overline{M}_{conv}$) and the large-scale mass flux, and (b) between the total mass flux in stratiform regions ($\overline{M}_{strt}$) and the large-scale mass flux. Lag times from −12 and +12 hours are calculated. Contours greater than 0.6 are hatched. Negative values are shown dashed.

contribute to $\overline{M}$, but at different levels, such a result indicates that $\overline{M}_{strt}$ lags $\overline{M}_{conv}$ by less than one wave-phase category. Therefore, the vertical structure of $\overline{M}$ (Fig. 6(a)) is highly related with both convective and stratiform processes, with convective processes preceding stratiform processes.

The areal percentages of the convective and stratiform columns and the associated surface precipitation rates are shown in Fig. 8. The convective precipitation rates are generally higher than the stratiform precipitation rates at any phase (Fig. 8(a)). This agrees qualitatively with the ratio for individual MCSs observed during GATE phase III (Leary and Houze 1980). The ratio of stratiform to convective precipitation rates becomes larger as the wave matures. This is intuitively correct because it is ascribed to the phase lag of the stratiform precipitation.

The percentage of convective columns is almost independent of wave phase with a magnitude of 6–8% (Fig. 8(b)). However, that of stratiform columns is strongly phase-dependent, and is largest between N and S. It is not surprising that the percentage of stratiform columns is more than two or three times higher than that of convective columns for most wave phases. The areal percentage of the convective columns is, however, much larger than that of the updraught area at a given height (1–2%) and that observed for individual MCSs (Leary and Houze 1980). Presence of shallow convection and updraughts of various life stages are probably responsible for the high areal percentage of the convective columns. Incorrect identification of convective column by the partitioning method (Xu 1995) cannot be ruled out.

(d)   Heat and moisture budgets

The heat and moisture budgets include two major components: the eddy heat- and moisture-flux convergences, and the phase changes. These two components cannot be separated in observational studies. Such a separation is essential to understand the role of cumulus convection in the easterly waves. The phase-change term in the heat budget is conventionally called latent-heat release, which includes condensation/evaporation,
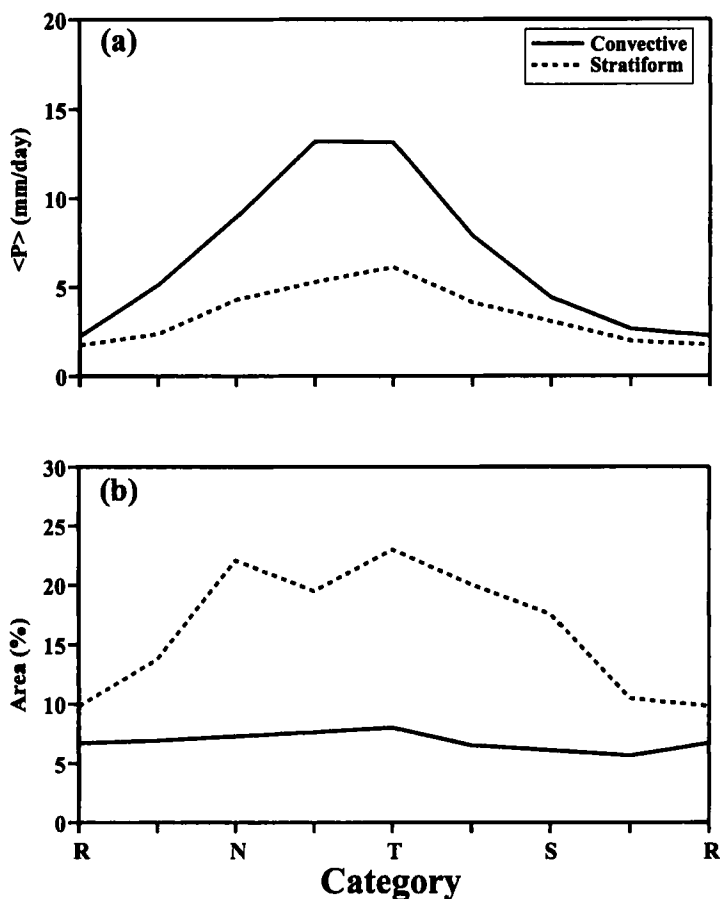
Figure 8. (a) The surface precipitation rate in convective and stratiform regions and (b) the associated areal coverage. See text for explanation of phase categories.

freezing/melting, and deposition/sublimation. In the moisture budget, only condensation/evaporation and deposition/sublimation are included. A complete list of equations can be found, for example, in Xu (1995).

A surprising feature appearing in Fig. 9(a) is that the latent-heat release exhibits two maxima, one in the lower troposphere before the trough phase, and the other above the freezing level at the trough phase. The former is related to condensation associated with convective updraughts. The latter is related to the freezing processes and probably reflects the phase lag of stratiform precipitation to convective precipitation. The phase-change term in the moisture budget (Fig. 9(b)) is expected to be similar to the latent-heat release except for the layer (4–5 km) around the melting level because the freezing/melting processes do not contribute to the phase-change rate in the moisture budget. The latent-heat release is also slightly larger in the upper troposphere because of the fusion effects. In addition, the evaporative cooling of rainwater is very large in the boundary layer.

It is not surprising that the eddy heat-flux convergences are one order of magnitude smaller than the latent-heat release (Fig. 9(c)) except in the boundary layer. This is ascribed to the small vertical potential-temperature gradients in the tropics and possibly to the pattern smoothing from compositing. In spite of their small magnitudes, the
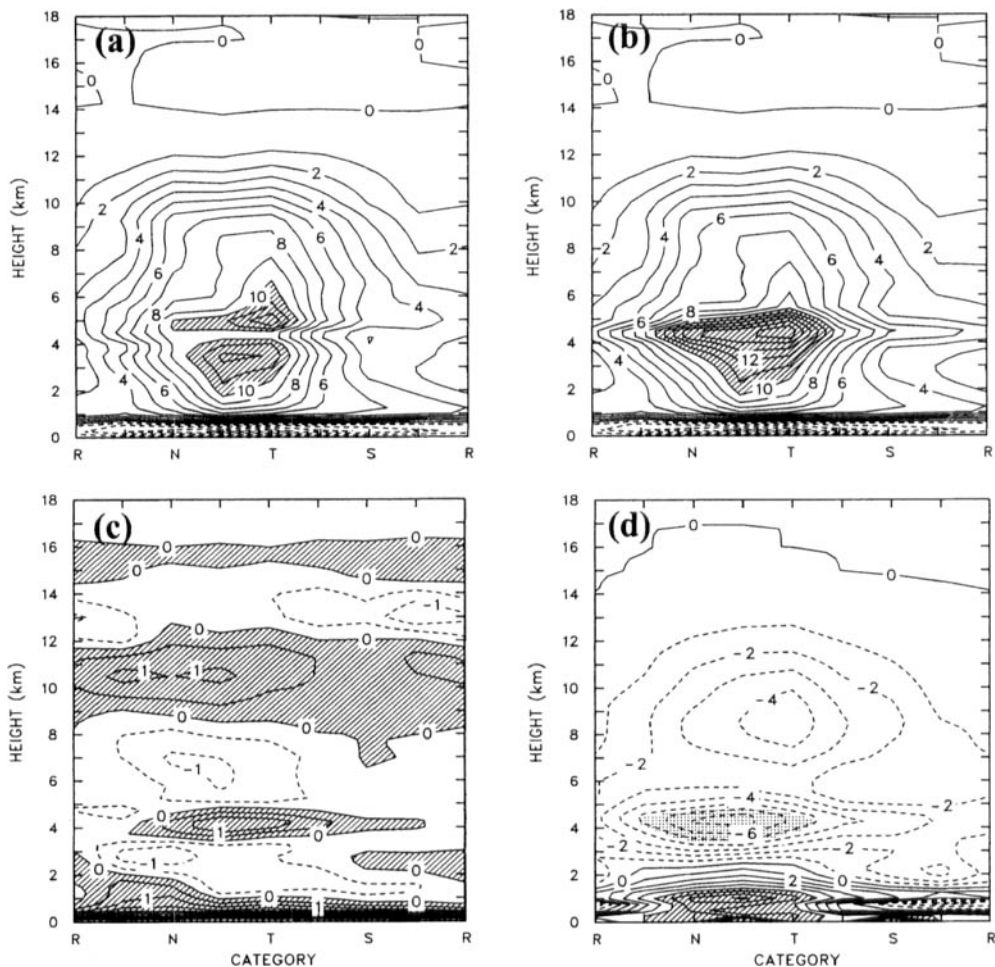
Figure 9. Wave phase–vertical cross-sections of the phase-change rates ((a) and (b)) and the convergences of eddy transports ((c) and (d)) in the heat ((a) and (c)) and moisture ((b) and (d)) budgets. Contour interval is 1 K day^{-1} with negative values shown dashed. Contours greater than 10 K day^{-1} are hatched in (a) and (b). In (c), contours greater than 0 K day^{-1} are hatched. Contours greater (less) than 5 (−5) K day^{-1} are hatched (dotted) in (d). See text for explanation of phase categories.

vertical structures are very complicated but in good agreement with the 3-D simulation of Donner *et al.* (1999). The large magnitudes in the boundary layer compensate the evaporative cooling of rainwater in the heat budget (Fig. 9(a)).

It is also not surprising that the eddy moisture-flux convergences have much simpler vertical structures and larger and comparable (to the phase-change term) magnitudes (Fig. 9(d)) because of the large vertical gradient of water vapour mixing ratio. Eddy transports by updraughts moisten the middle and upper troposphere while those by downdraughts dry the lower troposphere. There are two minima above 4 km, which also agrees with the 3-D simulation of Donner *et al.* (1999). Note that negative values correspond to moistening. The drying effects in the lower troposphere (below 2.5 km) are as large as the moistening effects around 4 km. Both are most likely related to the convective processes since they almost disappear after the trough phase when stratiform precipitation processes become more dominant (Fig. 8(a)). The other moistening centre
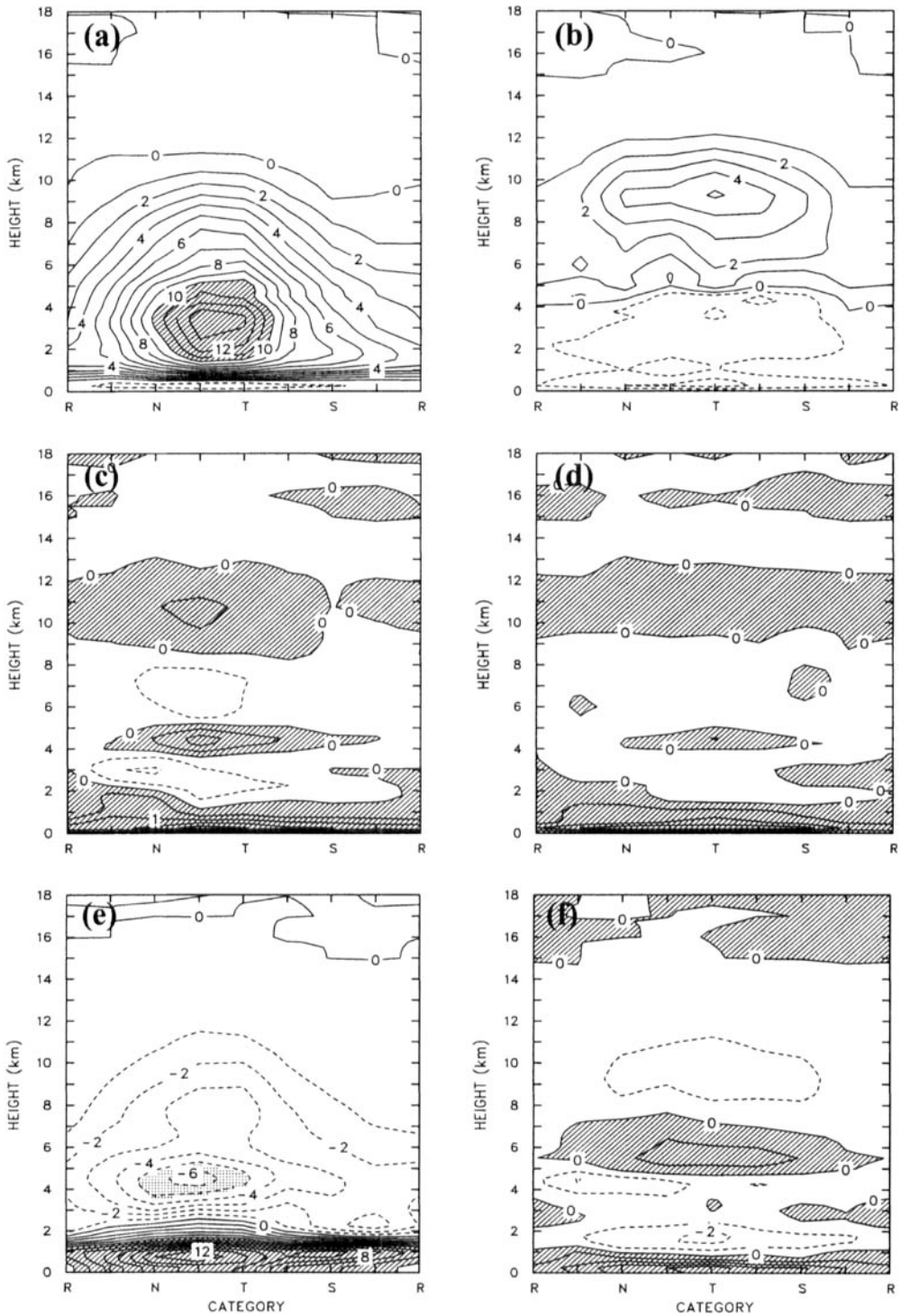
Figure 10. Same as Fig. 9 except for partitioning into convective (left panels) and stratiform (right panels) regions for latent-heat release ((a) and (b)), the convergences of eddy heat transports ((c) and (d)) and the convergence of eddy moisture transports ((e) and (f)).

appearing at ~9 km around the trough phase is probably related to both convective and stratiform processes.

The important conclusions from the examination of Fig. 9 are (i) that the diabatic heating in the composite easterly wave is dominated by the latent-heat release in the free atmosphere, and (ii) that the eddy transport convergences of moisture are equally important in the moisture budget. The latter has been ignored by most theoretical studies of easterly waves; for example, ignoring the moisture equation in the mathematical framework.

The differences between convective and stratiform processes can be further examined from the budget components: the latent-heat release, and the eddy heat- and moisture-transport convergences (Fig. 10). Although the magnitudes of all budget components in the stratiform regions are generally smaller than their counterparts in the convective regions, these budget components exhibit distinct vertical structures from those in the convective regions. The details are explained below.

Convective processes contribute greatly to the total latent-heat release in the early phases of the easterly waves. The distribution of latent-heat release by convective processes is rather similar to that of $\overline{M}_{conv}$ (Figs. 10(a) and 6), with the maximum appearing one phase before the trough. The largest magnitudes in the eddy transport convergences/divergences occur between N and T (Figs. 10(c) and (e)). That is, the eddy heat- and moisture-transport convergences also play more important roles in the early phases than in the late phases of the composite easterly wave.

Stratiform processes produce latent heating above the melting levels and cooling below the melting levels (Fig. 10(b)). Such a vertical latent-heating structure is consistent with the mass budget components discussed in section 3(c) (Fig. 6(c)) and distinct from that of convective regions. Although the contribution of mesoscale vertical transports to the heat and moisture budgets is smaller than that in convective regions, significantly different moisture-transport structures appear around 6 km; that is, the drying maximum (Fig. 10(f)). The two moistening maxima in the domain-averaged eddy moisture-transport convergences (Fig. 9(d)) are caused by this drying maximum.

An important conclusion from the results shown in Fig. 10 is that mesoscale stratiform processes, including the vertical transport convergences, should be separately included in formulating the representation of the collective effects of cumulus convection (e.g. Donner 1993; Alexander and Cotton 1998) because of their distinct vertical structures from those in convective regions. This conclusion is also supported by the mass budget analysis presented earlier and is consistent with that obtained by Xu (1995).

Another important feature shown in Fig. 10 is that the phase difference between the maximum convective and stratiform activities is also exhibited in all budget components, especially in the phase-change terms. The phase difference can be as long as two wave-phase categories (~24 h). This again indicates the importance of stratiform precipitation processes in the easterly waves, which has never been considered in theoretical studies. Therefore, the distinct vertical structures and the phase delays of stratiform processes (relative to convective processes) should be considered in future theoretical studies of the easterly waves and other waves in the tropics.

4. CONCLUSIONS

The mass, heat and moisture budgets of a composite easterly wave over the eastern tropical Atlantic have been analysed from simulations of a convection-resolving model (CRM), driven by observed synoptic-scale advective tendencies of heat and moisture

during GATE phase III. The compositing procedure for the simulated easterly waves is identical to that used in the observational study of Thompson *et al.* (1979).

The vertical structures and life cycles of the simulated, composite easterly wave are reasonably comparable with the observed, except for the lack of shallow convection embedded in the easterly waves. Although it has been known that mesoscale stratiform precipitation processes are an inseparable component of cumulus convection, especially for organized convective systems, the importance of mesoscale stratiform processes in the easterly waves has not received much attention. This study has identified two main differences of mesoscale stratiform processes from convective processes embedded in the easterly waves: (1) the distinct vertical structures of the mass, heat and moisture budget components due to mesoscale updraughts and downdraughts, and (2) the phase lags relative to the convective processes in the temporal evolution of the easterly waves. The phase differences between the peak convective and stratiform activities range from a few hours to $1\frac{1}{2}$ days in different budget components. The interrelationships among the different budget components have also been examined to illustrate the importance of mesoscale stratiform processes in the budgets of a composite easterly wave.

Based upon the findings of this study, it is strongly recommended that future theoretical studies should include both convective and mesoscale stratiform precipitation processes; this should lead to a better understanding of diabatic processes in the dynamics of the easterly waves and possibly other waves in the tropics.

As a by-product of this study, the detailed budget analysis for convective and stratiform regions of the composite easterly wave is valuable for evaluating the recently developed parametrizations that explicitly treat the stratiform precipitation, in particular, the individual components in the heat and moisture budgets.

Although 2-D simulations of cloud ensembles have some limitations, the agreement of our results with those of a similar 3-D simulation (Donner *et al.* 1999) is remarkably good in terms of the vertical structures of some budget components. Further improvements of the model physics is needed to simulate shallow cumulus convection better.

REFERENCES

Alexander, G. D. and Cotton, W. R.   1998   The use of cloud-resolving simulations of mesoscale convective systems to build a mesoscale parameterization scheme. *J. Atmos. Sci.*, **55**, 2137–2161

Betts, A. K. and Miller, M. J.   1986   A new convective adjustment scheme. Part II: Single column tests using GATE wave, BOMEX, ATEX and arctic air-mass data sets. *Q. J. R. Meteorol. Soc.*, **112**, 692–709

Burpee, R. W.   1972   The origin and structure of easterly waves in the lower troposphere of north Africa. *J. Atmos. Sci.*, **29**, 77–90

   1974   Characteristics of north African disturbances during the summer of 1968 and 1969. *J. Atmos. Sci.*, **31**, 1556–1570

Cahalan, R. F., Silberstein, D. and Snider, J. B.   1995   A validation of a satellite cloud retrieval during ASTEX. *J. Atmos. Sci.*, **52**, 3002–3012

Carlson, T. N.   1969   Some remarks on African disturbances and their progress over the tropical Atlantic. *Mon. Weather Rev.*, **97**, 716–726

Céron, J. P. and Guérémy, J. F. 1999 Validation of the space–time variability of African easterly waves simulated by the CNRM GCM. *J. Climate*, **12**, 2831–2855

Charney, J. G. and Eliassen, A. 1964 On the growth of the hurricane depression. *J. Atmos. Sci.*, **21**, 68–75

Chen, Y.-L. and Ogura, Y. 1982 Modulation of convective activity by large-scale flow patterns observed in GATE. *J. Atmos. Sci.*, **39**, 1260–1279

Donner, L. J. 1993 A cumulus parameterization including mass fluxes, vertical momentum dynamics, and mesoscale effects. *J. Atmos. Sci.*, **50**, 889–906

Donner, L. J., Seman, C. J. and Hemler, R. S. 1999 Three-dimensional cloud-system modeling of GATE convection. *J. Atmos. Sci.*, **56**, 1885–1912

Druyan, L. M. and Hall, T. M. 1994 Studies of African wave disturbances with the GISS GCM. *J. Climate*, **7**, 261–276

Duvel, J. P. 1990 Convection over tropical Africa and the Atlantic Ocean during northern summer. Part II: Modulation by easterly waves. *Mon. Weather Rev.*, **118**, 1855–1868

Estoque, M. A., Shukla, J. and Jing, J. C. 1983 African wave disturbances in a general circulation model. *Tellus*, **35A**, 287–295

Fowler, L. D., Randall, D. A. and Rutledge, S. A. 1996 Liquid and ice cloud microphysics in the CSU general circulation model. Part I: Model description and simulated microphysical processes. *J. Climate*, **9**, 489–529

Fyfe, J. C. 1999 Climate simulations of African easterly waves. *J. Climate*, **12**, 1747–1769

Ghan, S., Randall, D. A., Xu, K.-M., Cederwall, R., Cripe, D., Hack, J., Iacobellis, S., Klein, S., Krueger, S., Lohmann, U., Pedretti, J., Robock, A., Rotstayn, L., Somerville, R., Stenchikov, G., Sud, Y., Walker, G., Xie, S., Yio, J. and Zhang, M. 2000 An intercomparison of single column model simulations of summertime midlatitude continental convection. *J. Geophys. Res.*, **105**, 2091–2124

Grabowski, W. W., Wu, X. and Moncrieff, M. W. 1996 Cloud-resolving modeling of tropical cloud systems during phase III of the GATE. Part I: Two-dimensional experiments. *J. Atmos. Sci.*, **53**, 3684–3709

Gregory, D. and Rowntree, P. R. 1990 A mass flux convection scheme with representation of cloud ensemble characteristics and stability-dependent closure. *Mon. Weather Rev.*, **118**, 1483–1506

Harshvardhan, Wielicki, B. A. and Ginger, K. M. 1994 The interpretation of remotely sensed cloud properties from a model parameterization perspective. *J. Climate*, **7**, 1987–1998

Holton, J. R. 1971 A diagnostic model for equatorial wave disturbances: The role of vertical shear of the mean zonal wind. *J. Atmos. Sci.*, **28**, 55–64

Houze Jr, R. A. 1977 Structure and dynamics of a tropical squall-line system. *Mon. Weather Rev.*, **105**, 1540–1567

Hudlow, M. D. and Patterson, V. L. 1979 *GATE radar rainfall atlas*. NOAA special report. US Government Printing Office, Washington, DC, USA

Krishnamurti, T. N., Wong, V., Pan, H. L., Van Dam, G. and McClellan, D. 1976 'Sea surface temperatures for GATE.' Report 76-3, Department of Meteorology, Florida State University, Tallahassee, FL, USA

Krueger, S. K. 1988 Numerical simulation of tropical cumulus clouds and their interaction with the subcloud layer. *J. Atmos. Sci.*, **45**, 2221–2250

Krueger, S. K., Fu, Q., Liou, K. N. and Chin, H.-N. 1995 Improvements of an ice-phase microphysics parameterization for use in numerical simulations of tropical convection. *J. Appl. Meteorol.*, **34**, 281–287

Kwon, H. J. 1989 A reexamination of the genesis of African waves. *J. Atmos. Sci.*, **46**, 3621–3631

Kwon, H. J. and Mak, M. 1990 A study of the structural transformation of the African easterly waves. *J. Atmos. Sci.*, **47**, 277–292

Landsea, C. W. 1993 A climatology of intense (or major) Atlantic hurricanes. *Mon. Weather Rev.*, **121**, 1703–1713

Lau, K.-H. and Lau, N.-C. 1990 Observed structure and propagation characteristics of tropical summertime synoptic-scale disturbances. *Mon. Weather Rev.*, **118**, 1888–1913

Lau, K.-H. and Lau, N.-C.	1992	The energetics and propagation dynamics of tropical summertime synoptic-scale disturbances. *Mon. Weather Rev.*, **120**, 2523–2539
Leary, C. A. and Houze, Jr, R. A.	1980	The contribution of mesoscale motions to the mass and heat fluxes of an intense tropical convective system. *J. Atmos. Sci.*, **37**, 784–796
Lindzen, R. S.	1974	Wave-CISK in the tropics. *J. Atmos. Sci.*, **31**, 156–179
Lipps, F. B. and Hemler, R. S.	1986	Numerical simulation of deep tropical convection associated with large-scale convergence. *J. Atmos. Sci.*, **43**, 1796–1816
Lord, S. J. and Arakawa, A.	1980	Interaction of a cumulus cloud ensemble with the large-scale environment. Part II. *J. Atmos. Sci.*, **37**, 2677–2692
Mass, C.	1979	A linear primitive equation model of African wave disturbances. *J. Atmos. Sci.*, **36**, 2075–2092
Nitta, T.	1970	A study of generation and conversion of eddy available potential energy in the tropics. *J. Meteorol. Soc. Japan*, **48**, 524–528
Norquist, D. C., Recker, E. E. and Reed, R. J.	1977	The energetics of African wave disturbances as observed during phase III of GATE. *Mon. Weather Rev.*, **105**, 334–342
Ooyama, K.	1964	A dynamical model for the study of tropical cyclone development. *Geofis. Int.*, **4**, 187–198
Paradis, D., Redelsperger, J.-L. and Balaji, V.	1995	African easterly waves and convection. Part I: Linear simulations. *J. Atmos. Sci.*, **52**, 1657–1679
Poore, K. D., Wang, J. and Rossow, R. B.	1995	Cloud layer thickness from a combination of surface and upper-air observations. *J. Climate*, **8**, 550–568
Reed, R. J. and Recker, E. E.	1971	Structure and properties of synoptic-scale wave disturbances in the equatorial Western Pacific. *J. Atmos. Sci.*, **28**, 1117–1133
Reed, R. J., Norquist, D. C. and Recker, E. E.	1977	The structure and properties of African wave disturbances as observed during phase III of GATE. *Mon. Weather Rev.*, **105**, 317–333
Reed, R. J., Hollingsworth, A., Heckley, W. A. and Delsol, F.	1988	An evaluation of the performance of the ECMWF operational system in analyzing and forecasting easterly wave disturbances over Africa and the tropical Atlantic. *Mon. Weather Rev.*, **116**, 824–865
Rennick, M. A.	1976	The generation of African waves. *J. Atmos. Sci.*, **33**, 1955–1969
Rhiel, H.	1954	*Tropical meteorology.* McGraw-Hill
Shapiro, L., Stevens, D. E. and Ciesilski, P. E.	1988	A comparison of observed and model-derived structures of Caribbean easterly waves. *Mon. Weather Rev.*, **116**, 921–938
Simmons, A. J.	1977	A note on the instability of the African easterly jet. *J. Atmos. Sci.*, **34**, 1670–1674
Soong, S.-T. and Tao, W.-K.	1980	Response of deep tropical cumulus clouds to mesoscale processes. *J. Atmos. Sci.*, **37**, 2016–2034
Tao, W.-K. and Soong, S.-T.	1986	A study of the response of deep tropical clouds to mesoscale processes: Three-dimensional numerical experiments. *J. Atmos. Sci.*, **43**, 2653–2676
Thompson Jr, R. M., Payne, S. W., Recker, E. E. and Reed, R. J.	1979	Structure and properties of synoptic-scale wave disturbances in the intratropical convergence zone of the eastern Atlantic. *J. Atmos. Sci.*, **36**, 53–72
Thorncroft, C. D.	1995	An idealized study of African easterly waves. III: More realistic basic states. *Q. J. R. Meteorol. Soc.*, **121**, 1589–1614
Thorncroft, C. D. and Hoskins, B. J.	1994a	An idealized study of African easterly waves. I: A linear view. *Q. J. R. Meteorol. Soc.*, **120**, 953–982
	1994b	An idealized study of African easterly waves. II: A nonlinear view. *Q. J. R. Meteorol. Soc.*, **120**, 983–1015
Tiedtke, M.	1989	A comprehensive mass flux scheme for cumulus parameterization in large-scale models. *Mon. Weather Rev.*, **117**, 1779–1800
Xu, K.-M.	1995	Partitioning mass, heat and moisture budgets of explicitly simulated cumulus ensembles into convective and stratiform components. *J. Atmos. Sci.*, **52**, 551–573
Xu, K.-M. and Krueger, S. K.	1991	Evaluation of cloudiness parameterizations using a cumulus ensemble model. *Mon. Weather Rev.*, **119**, 342–367
Xu, K.-M. and Randall, D. A.	1995	Impact of interactive radiative transfer on the macroscopic behavior of cumulus ensembles. Part I: Radiation parameterization and sensitivity tests. *J. Atmos. Sci.*, **52**, 785–799
	1996	Explicit simulation of cumulus ensembles with the GATE phase III data: Comparison with observations. *J. Atmos. Sci.*, **53**, 3710–3736
Xu, K.-M., Arakawa, A. and Krueger, S. K.	1992	The macroscopic behavior of cumulus ensembles simulated by a cumulus ensemble model. *J. Atmos. Sci.*, **49**, 2402–2420